

Complex mantle flow in the Mariana subduction system: evidence from shear wave splitting

S. H. Pozgay,¹ D. A. Wiens,¹ J. A. Conder,¹ H. Shiobara² and H. Sugioka³

¹Washington University in St. Louis, Department of Earth and Planetary Sciences, 1 Brookings Drive, St. Louis, MO 63130, USA. E-mail: spozgay@wustl.edu

²Earthquake Research Institute, University of Tokyo 1-1-1 Yayoi, Bunkyo-ku, Tokyo 113-0032, Japan

³IFREE, JAMSTEC, 2-15 Natsushima-Cho, Yokosuka 237-0061, Japan

Accepted 2007 March 2, Received 2007 March 1; in original form 2006 November 14

SUMMARY

Shear wave splitting measurements provide significant information about subduction zone mantle flow, which is closely tied to plate motions, lithospheric deformation, arc volcanism, and backarc spreading processes. We analyse the shear wave splitting of local *S* waves recorded by a large 2003–2004 deployment consisting of 58 ocean-bottom seismographs (OBSs) and 20 land stations and by nine OBSs from a smaller 2001–2002 deployment. We employ several methods and data processing schemes, including spatial averaging methods, to obtain stable and consistent shear wave splitting patterns throughout the arc–backarc system. Observed fast orientation solutions are dependent on event location and depth, suggesting that anisotropic fabric in the mantle wedge is highly heterogeneous. Shear waves sampling beneath the northern island arc (latitudes 17.5°–19°N) and between the arc and backarc spreading centre show arc-parallel fast orientations for events shallower than 250 km depth; whereas, fast orientations at the same stations are somewhat different for deeper events. Waves sampling beneath the central island arc stations (latitudes 15.5°–17.5°) show fast orientations subparallel to both the arc and absolute plate motion (APM) for events <250 km depth and APM-parallel for deeper events. Ray paths sampling west of the spreading centre show fast orientations ranging from arc-perpendicular to APM-parallel. Arc-parallel fast orientations characterize the southern part of the arc with variable orientations surrounding Guam. These results suggest that the typical interpretation of mantle wedge flow strongly coupled to the downgoing slab is valid only at depths greater than ~250 km and at large distances from the trench. We conclude that the arc-parallel fast orientations are likely the result of physical arc-parallel mantle flow and are not due to recently proposed alternative lattice preferred orientation mechanisms and fabrics. This flow pattern may result from along-strike pressure gradients in the mantle wedge, possibly due to changes in slab dip and/or convergence angles.

Key words: Mariana Islands, seismic anisotropy, shear wave splitting, subduction zone.

1 INTRODUCTION

The flow pattern of subduction zone mantle wedges is a matter of great importance for understanding the dynamics of subduction and backarc spreading processes. Models of subduction systems suggest that mantle wedge flow may be dominated by viscous coupling to the downgoing slab, producing flow directions parallel to the present-day absolute plate motion (APM) of the downgoing plate (McKenzie 1979; Ribe 1989; van Keken 2003). However, more complex flow patterns, including arc-parallel flow above the slab, may be produced by significant amounts of slab rollback (Buttles & Olson 1998), shearing or extension in the arc-parallel direction (Hall *et al.* 2000), changes in slab dip (Buttles & Olson 1998; Hall *et al.* 2000), or changes in convergence angle (Blackman & Kendall 2002; Honda & Yoshida 2005). Mantle flow may also align parallel to the

orientation of maximum extension beneath the backarc spreading centre (Fischer *et al.* 2000).

It is commonly assumed that observations of seismic anisotropy can provide strong constraints on mantle flow patterns. Both petro-physical studies of mantle xenoliths (Nicolas & Christensen 1987; Mainprice & Silver 1993) and laboratory studies of deforming rocks (Zhang & Karato 1995; Zhang *et al.* 2000) suggest that, in most cases, flow of mantle materials should produce a ‘fast orientation’ of upper-mantle anisotropy aligned close to or along the flow orientation, although some recent studies suggest that under a restricted range of conditions such as high stress and high water content, the ‘fast orientation’ may be perpendicular to the flow direction (Jung & Karato 2001; Karato 2003).

The Mariana subduction system is a highly complex tectonic environment. Active volcanism throughout the forearc, arc and backarc

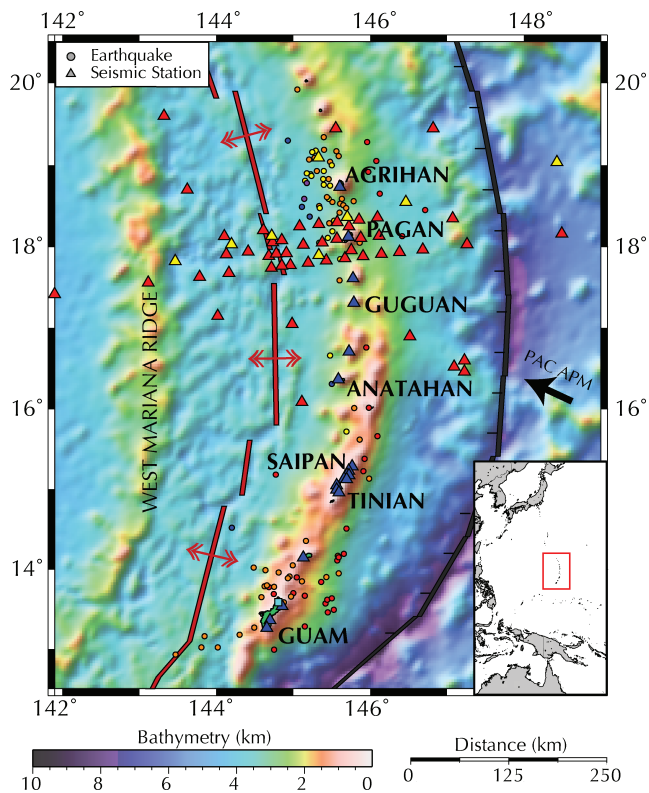


Figure 1. Bathymetric station map of Mariana Islands, the location of which is enclosed by the red box in the small inset. Blue triangles are broadband land stations, red triangles are 2003–2004 OBSs that returned data (see Table 1), yellow triangles are 2001–2002 OBSs used in the current study. Large black vector is Pacific plate absolute plate motion (PAC APM). The backarc spreading centre and trench are sketched with thick red and black lines. Spreading direction is perpendicular to the spreading ridges, as indicated by small double-headed red arrows. Several islands are named in bold text. Blue square on Guam is GSN station GUMO. Earthquakes (circles) are colour coded by increasing depth: <100 km are red, 100–200 km orange, 200–300 km yellow, 300–400 km green, 400–500 km blue and >500 km violet.

spreading centre, in addition to significant along-strike changes in slab dip and convergence angles, suggest complicated patterns of mantle flow throughout the region. However, the Marianas are commonly cited as having mantle flow parallel to present-day Pacific Plate APM directions based on prior studies at Guam (Xie 1992; Fouch & Fischer 1998). Here we analyse shear wave splitting results from two well-distributed seismograph deployments to characterize mantle flow patterns throughout the Mariana arc system. We find that several mechanisms are required to explain the observed shear wave splitting patterns and that the conventional corner flow model in a subduction zone is not a comprehensive description of mantle flow in the Mariana system.

1.1 Regional setting

The Mariana arc system encompasses a wide variety of tectonic settings, with active serpentinite seamounts in the forearc, an active island arc and backarc spreading centre, and an extinct fossil arc on the overriding Philippine Sea Plate (Fig. 1). Geochemical variations have been observed across and along the arc (Kelley *et al.* 2003; Pearce *et al.* 2005) and several physical features change rapidly along strike of the arc. Near Pagan, the slab dip is nearly vertical

and the slab appears to penetrate the 660 km discontinuity (van der Hilst *et al.* 1991). Convergence is highly oblique at a rate of $\sim 4 \text{ cm yr}^{-1}$ and the half spreading rate at the Mariana trough is $\sim 1.6 \text{ cm yr}^{-1}$ (Kato *et al.* 2003). The southern part of the arc near Guam and Rota is significantly different from the northern part of the arc. The slab dips at $\sim 55^\circ$, seismicity extends only to depths of $\sim 250 \text{ km}$, and convergence is roughly perpendicular to the trench at a rate of $\sim 6.5 \text{ cm yr}^{-1}$ (Stern *et al.* 2003). The half spreading rate of the southern Mariana trough is $\sim 4.5 \text{ cm yr}^{-1}$ (Kato *et al.* 2003). The Mariana trench does not experience rollback (Stern *et al.* 2003), as both the trench and the overriding Philippine Sea Plate both move westward at rates of $\sim 2.5\text{--}5$ and $\sim 3\text{--}8 \text{ cm yr}^{-1}$, respectively (Heuret & Lallemand 2005; Martinez *et al.* 2000). Upper plate and trench migration rates are maximum near Saipan and Tinian Islands and backarc spreading rates are maximum near Guam (Martinez *et al.* 2000). Plate motions suggest that backarc deformation is primarily controlled by upper plate motions (Heuret & Lallemand 2005).

1.2 Previous work

Despite the intrinsic value of shear wave splitting measurements for addressing questions regarding the flow pattern in the Mariana mantle wedge, prior observations are sparse with data obtained only at the Global Seismic Network (GSN) station on Guam (GUMO) and a few ocean-bottom seismographs (OBSs) (Xie 1992; Fouch & Fischer 1998; Volti *et al.* 2006). These studies found fast orientations roughly parallel to the Pacific plate APM orientation and attributed their observations to the conventional interpretation of mantle wedge corner flow. The one exception to this is near the backarc spreading centre, where Volti *et al.* (2006) found fast orientations subparallel to the spreading direction.

The present study provides a detailed and thorough analysis of shear wave splitting patterns observed along and across the entire Mariana arc system. We use a relatively dense deployment of land and ocean bottom seismographs (Fig. 1) and analyse local *S* phases with multiple data processing schemes to describe mantle flow patterns throughout the region. We find that while the commonly cited APM-parallel fast orientations are present in certain areas, arc-parallel fast orientations dominate at shallow and intermediate depths. Results show that mantle flow patterns vary along-strike of the arc and in the across-arc direction, indicating that a simple corner flow model for the region is not ubiquitous.

2 DATA AND METHODS

2.1 Data acquisition

Two seismic deployments provide a high-resolution data set for this study. Most data is from the 2003–2004 MultiScale Seismic Imaging Experiment in the Mariana Subduction System consisting of an 11-month deployment of 20 land broadband seismographs and 58 semi-broadband OBSs (Fig. 1 and Table 1). The 78 stations were deployed during 2003 May–June and recovered during 2004 April–May. The land stations used Streckheisen STS-2 and Guralp CMG-40T sensors and were deployed on each island between Guam and Agrihan, with Reftek 72A-08 dataloggers and GPS timing. The 58 OBSs surround the deepest earthquake locations near Pagan Island and traverse the trench, forearc, island arc, and backarc spreading centre, extending across the West Mariana Ridge. Fifty OBSs used three-component Mark Products L4 sensors with 1 Hz natural period and modified amplifiers to extend long-period performance

Table 1. Station information for 2001–2002 and 2003–2004 deployments. Land stations are listed by island name; OBS stations are listed by OBS number. Data recovery problems are noted in the table and are discussed in the text. OBSs never recovered are not listed.

Station	Latitude (°)	Longitude (°)	Elevation (m)	Type ^a	On date	Off date	Results ^b
Agrihan	18.7365	145.6529	71	STS-2	05/10/03	04/18/04	A
Alamagan	17.6124	145.8214	71	STS-2	05/08/03	04/22/04	S
Anatahan	16.3644	145.6337	91	STS-2	05/06/03	04/15/04	A
Guam	13.5397	144.9140	289	CMG-40T	05/06/03	05/14/04	A
Guam	13.3631	144.7592	163	CMG-40T	05/08/03	05/14/04	A
Guam	13.2664	144.7172	140	STS-2	05/08/03	05/15/04	A
Guguan	17.3116	145.8334	80	STS-2	05/07/03	04/23/04	A
MAR01	17.2331	141.3855	−4731	PMD	10/09/01	10/06/02	S
MAR02	17.8251	143.5433	−5171	PMD	10/09/01	10/06/02	S
MAR03	18.0333	144.2667	−3811	PMD	10/09/01	09/15/02	S
MAR04	18.1314	144.7814	−3478	PMD	10/09/01	09/15/02	A
MAR05	18.3660	145.7503	−2728	PMD	10/09/01	10/06/02	A
MAR06	18.5501	146.4986	−3698	PMD	10/09/01	09/27/02	S
MAR07	19.0362	148.4356	−5557	PMD	10/09/01	10/01/02	A
MAR08	17.8992	145.3837	−3509	PMD	10/09/01	10/01/02	A
MAR09	19.0918	145.3807	−3571	PMD	10/09/01	09/15/02	A
PMD03	17.0504	145.0403	−3800	PMD	06/20/03	04/12/04	A
PMD04	17.1482	144.0892	−4326	PMD	06/21/03	04/11/04	S
PMD16	17.7750	145.0182	−3471	PMD	06/20/03	03/21/04	S
PMD22	17.9367	146.4181	−3417	PMD	06/18/03	04/02/04	S
PMD40	18.2053	144.6745	−3701	PMD	06/15/03	04/01/04	A
PMD42	18.2504	145.1378	−3744	PMD	06/15/03	04/02/04	A
PMD46	18.3581	146.1356	−3373	PMD	06/16/03	04/01/04	A
PMD58	17.4189	141.9958	−4474	PMD	06/22/03	03/11/04	A
OBS02	16.8998	146.5501	−3492	MPL4n	06/21/03	08/10/04	A
OBS06	16.0834	145.1657	−3608	MPL4n	06/23/03	07/30/03	A
OBS07	16.4604	147.2519	−3224	MPL4n	06/20/03	05/11/04	S
OBS08	16.5206	147.1191	−3541	MPL4o	06/21/03	05/11/04	S
OBS09	16.6002	147.2499	−3334	MPL4o	06/21/03	05/10/04	S
OBS10	17.5614	143.1964	−2418	MPL4n	06/23/03	08/09/03	A
OBS11	17.6302	143.8577	−3889	MPL4n	06/23/03	08/09/03	N
OBS12	17.6787	144.2322	−3948	MPL4n	06/23/03	06/29/03	S
OBS14	17.7444	144.7780	−3671	MPL4o	06/23/03	05/02/04	S
OBS15	17.7677	144.9094	−4152	MPL4n	06/22/03	07/31/03	N
OBS17	17.8033	145.2489	−3595	MPL4n	06/22/03	07/31/03	N
OBS18	17.8327	145.4807	−3244	MPL4n	06/21/03	07/31/03	N
OBS19	17.8596	145.7184	−2882	MPL4o	06/22/03	05/06/04	A
OBS20	17.8849	145.9510	−2702	MPL4n	06/22/03	05/08/04	N
OBS21	17.9114	146.1851	−2602	MPL4n	06/21/03	05/08/04	A
OBS23	17.9659	146.7163	−3491	MPL4o	06/20/03	05/08/04	A
OBS25	18.0333	147.2825	−3723	MPL4n	06/19/03	07/31/03	A
OBS26	18.1624	148.4979	−5923	MPL4n	06/18/03	07/01/03	A
OBS27	17.8892	144.7436	−3883	MPL4n	06/23/03	07/27/03	N
OBS28	17.9160	144.8410	−4624	MPL4o	06/23/03	05/03/04	A
OBS29	17.9239	144.9671	−3740	MPL4n	06/22/03	05/03/04	A
OBS31	18.0586	144.7900	−4386	MPL4n	06/16/03	07/31/03	A
OBS32	18.0809	144.9098	−3565	MPL4o	06/16/03	05/04/04	A
OBS33	17.9075	144.1975	−3847	MPL4o	06/16/03	05/01/04	A
OBS34	17.9398	144.4771	−3880	MPL4n	06/16/03	07/30/03	N
OBS35	18.0261	145.1856	−3688	MPL4n	06/22/03	05/06/04	N
OBS36	18.0541	145.4288	−3176	MPL4o	06/22/03	05/06/04	S
OBS37	18.1345	146.1582	−3034	MPL4n	06/18/03	05/08/04	N
OBS38	18.1297	144.1725	−4154	MPL4n	06/16/03	07/30/03	S
OBS43	18.2776	145.3837	−3338	MPL4n	06/18/03	07/31/03	N
OBS44	18.3042	145.6212	−2585	MPL4o	06/18/03	05/07/04	A
OBS45	18.3311	145.9002	−2669	MPL4n	06/18/03	05/07/04	S
OBS47	18.2496	145.7710	−1898	MPL4o	06/18/03	05/07/04	A
OBS48	18.1085	145.9230	−2247	MPL4o	06/18/03	05/07/04	A
OBS49	17.9595	145.7990	−2287	MPL4o	06/22/03	05/08/04	A
OBS50	18.0978	145.6150	−2339	MPL4n	06/21/03	05/07/04	N
OBS51	18.3497	147.1013	−2757	MPL4n	06/19/03	05/09/04	S
OBS52	19.4504	145.6001	−2475	MPL4n	06/17/03	05/05/04	N
OBS53	18.7006	143.6993	−3656	MPL4n	06/16/03	07/30/03	N

Table 1. (Continued.)

Station	Latitude (°)	Longitude (°)	Elevation (m)	Type ^a	On date	Off date	Results ^b
OBS54	18.7009	144.8001	-4139	MPL4n	06/17/03	05/04/04	N
OBS55	19.4498	146.8497	-4735	MPL4n	06/18/03	07/25/03	A
OBS57	19.5999	143.4003	-4070	MPL4n	06/16/03	07/30/03	A
Pagan	18.1207	145.7669	73	STS-2	05/25/03	04/16/04	A
Pagan	18.1222	145.7617	61	STS-2	05/09/03	04/17/07	A
Rota	14.1481	145.1866	528	STS-2	05/10/03	05/05/04	A
Saipan	15.2857	145.8093	100	STS-2	04/30/03	05/01/04	A
Saipan	15.2340	145.7670	219	CMG-40T	05/02/03	05/01/04	A
Saipan	15.1837	145.7466	410	STS-2	05/03/03	05/07/04	A
Saipan	15.1746	145.7712	116	CMG-40T	06/27/03	05/02/04	A
Saipan	15.1323	145.7076	74	CMG-40T	05/05/03	05/07/04	A
Saipan	15.1258	145.7409	122	CMG-40T	05/03/03	05/02/04	A
Sarigan	16.7096	145.7697	85	STS-2	05/06/03	04/24/04	A
Tinian	15.0484	145.6124	126	CMG-40T	05/16/03	05/03/04	A
Tinian	14.9950	145.6130	133	STS-2	05/15/03	05/04/04	A
Tinian	14.9604	145.6412	110	CMG-40T	05/15/03	05/04/04	A

^aStreckheisen STS-2, Guralp CMG-40T, Precision Measuring Devices (PMD), Lamont-Doherty Mark Products L-4 (MPL4n for new model, MPL4o for old model).

^b'A'—quality-A results reported, 'S'—some splitting results but no quality-A splitting measurements and 'N'—no usable splitting results (see text for discussion).

(Webb *et al.* 2001). Fifteen of these OBSs were an older 16-bit model and 35 of were a new 24-bit design, and they were operated by Lamont Doherty Earth Observatory (these instruments are denoted by the 'OBS' prefixes in Table 1). The remaining eight OBSs used Precision Measuring Devices (PMD – WB2023LP) sensors with a low frequency corner at 0.03 Hz and were built by H. Shiobara at the University of Tokyo (denoted by the 'PMD' prefixes in Table 1). The 35 new U.S. OBSs stopped recording data ~50 days after deployment due to a firmware error, eight U.S. OBSs were not recovered, and the Anatahan Island station had several power failures due to ash from the eruption covering the solar panels (see Pozgay *et al.* 2005). Several of the U.S. OBSs also failed to properly deploy the sensor to the seafloor. All other stations operated smoothly for the duration of the 2003–2004 deployment. The smaller data set is from nine OBSs with PMD sensors deployed during 2001–2002 across the arc system (denoted by the 'MAR' prefixes in Table 1) (Shiobara *et al.* 2005).

2.2 Data selection and processing

We use local earthquakes with depths greater than 80 km from the USA National Earthquake Information Center (NEIC) global catalog. Most events are between 100 and 300 km depth, but several events are between 300 and 600 km. We also investigated earthquakes located by the local deployment, but not identified at the NEIC due to their small magnitudes; only a few of these earthquakes were added to the final event list. Earthquake locations and depths were checked against relocations made using the local network. Unlike Volti *et al.* (2006) who used earthquakes as shallow as 19 km, we use only intermediate and deep earthquakes to eliminate complex ray propagation effects associated with shallow regional events and to provide ray paths that are generally propagating vertically. Most earthquakes have *S* arrivals within the shear wave window only at stations located fairly close to the events, which limits our sampling range. In addition, *S* arrivals west of the spreading centre experience higher attenuation than at stations east of the trough axis, such that only the larger events have high quality *S* arrivals in the far backarc. We also investigated *SKS* arrivals, but no reliable splitting

measurements were obtained due to low signal-to-noise ratio and poor distribution of events in the proper distance ranges. Finally, we compute shear wave splitting measurements for 59 OBSs and 20 land stations. The final 2003–2004 data set consists of 252 local events with 1232 event-station pairs and 25 events with 72 event-station pairs from the 2001–2002 deployment; a total of 79 stations, 277 events, and 1304 event-station pairs (Fig. 2 and Table 1).

Filtering is often necessary to eliminate noisy portions of the spectrum, particularly the microseism peak near 0.2 Hz and/or high frequencies that may result from near receiver scattering. Some frequency dependence has previously been reported in results observed at the GUMO station (Fouch & Fischer 1998). Therefore, we analyse each shear wave with three filters (a 1-Hz lowpass filter and bandpass filters at 0.3–0.7 and 0.5–1.5 Hz) and visually inspect them to determine which frequency band produced the best result. In many cases, only one filter (usually 0.3–0.7 Hz) is appropriate. For larger events with very high signal-to-noise ratio across the entire frequency band, the three filters produce nearly the same result.

We orient OBSs using polarization data from air-gun shots and several Rayleigh waves and average 7–15 high-quality measurements for each OBS to ensure accuracy of the final orientations. Standard errors for the orientations range from 3° to 7°, except for four OBSs with standard errors of 13°–17°. In total, we compute 27 OBS orientations and use two orientations determined from *P*-wave polarizations by Volti *et al.* (2006). Note that we only orient OBSs with quality-A splitting results (see below).

2.3 Shear wave splitting analysis

Shear wave splitting is the process by which an *S*-wave travelling through a seismically anisotropic medium is split into a fast component and an orthogonal slow component. Two parameters describe the effects of anisotropy on the waveform: the polarization orientation of the fast component (ϕ) measured in degrees clockwise from north and the time lag (δt) between the two components (see Savage 1999 for a review). (Although 'fast direction' is the predominant term throughout the literature, we in most cases refer to a

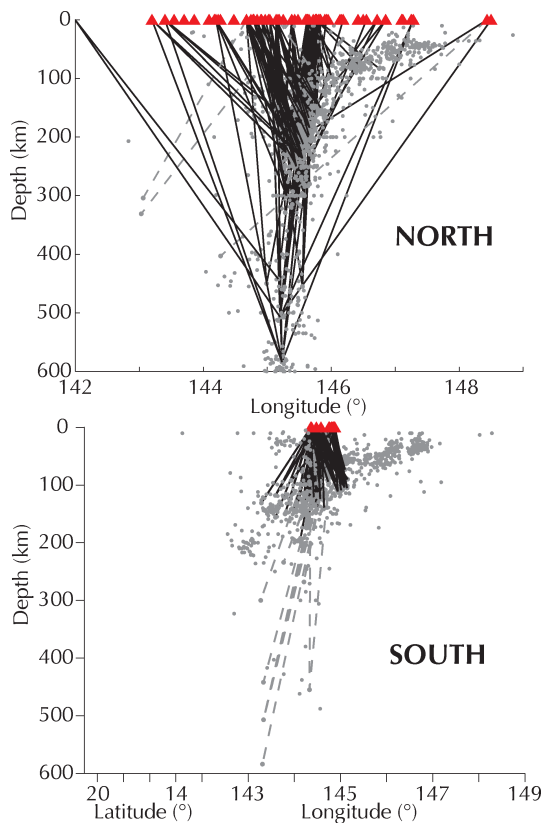


Figure 2. Cross-section of sketched ray paths. NORTH (top) and SOUTH (lower) regions are divided at 16°N latitude. Note that grey dashed lines in the NORTH panel are for events located in the southern or extreme northern region and do not plot along the slab contour for $16\text{--}19^{\circ}\text{N}$. For the SOUTH panel, grey dashed lines are from events in the northern region. Note that the orientation of the SOUTH panel is trench-perpendicular. Earthquakes delineating slab (grey circles) are events since 1976 in the NEIC database.

180° -ambiguous direction, and so use the term ‘orientation’.) Several methods, including a covariance matrix method (Silver & Chan 1988; Silver & Chan 1991) and a cross-correlation method (Fukao 1984; Bowman & Ando 1987) have been developed to determine the optimum splitting parameters. The covariance method solves for the most linear particle motion after correcting for arbitrary splitting by minimizing the second eigenvalue of the covariance matrix. In contrast, the cross-correlation method finds the maximum cross-correlation between corrected components.

There are significant differences in how shear wave splitting studies are carried out. Many studies use only one method without intercomparison with other methods, and some studies numerically select high quality results with a small amount of visual inspection. In addition, frequency dependence, noise, cycle skipping, and improper window lengths can bias shear wave splitting measurements. To make our measurements as systematic as possible and to reduce the effect of possible biases, we employ both above-mentioned analysis techniques, solve for the optimal window length and position and grade each result visually with numerical verification.

For each waveform, we compute splitting parameters with the covariance matrix method utilizing an automatic windowing scheme to solve for the most stable analysis window (Teaby *et al.* 2004). Initial window position begins 0.5 s before the arrival and ends 1.5 s after. The start and end times of the window are incremented by 0.35 and 0.3 s, respectively, such that absolute window lengths

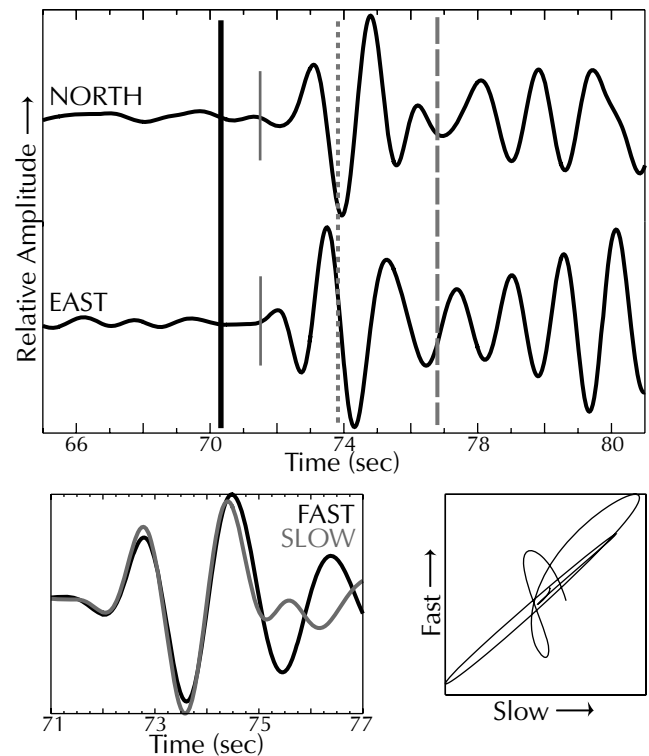


Figure 3. Cross-correlation solution for event on Julian day 179 of 2003 at 07:24.41 GMT at 18.354°N , 145.776°E , 143 km recorded at Guguan Island station. Filter is bandpass at 0.3–0.7 Hz. *Top*: unrotated seismograms. Short grey lines are S arrival picks, long heavy black line is start of analysis window, dotted line is end of covariance matrix window, and dashed line is end of cross-correlation window. *Bottom left*: corrected waveforms rotated to $\phi = -60^{\circ}$ and time shifted to $\delta t = 0.5$ s; *bottom right*: particle motion plot for corrected seismograms. The covariance matrix solution of $\phi = -59^{\circ}$ and $\delta t = 0.487$ s is identical to the cross-correlation solution and is not shown.

range from 2 to 10 s in length. Splitting parameters are computed for the covariance matrix method at each of the 175 window positions. The optimal solution is found using a hierarchical cluster analysis technique (Everitt 1993; Teaby *et al.* 2004).

Subsequent to automatic windowing computation of the covariance matrix solution, we compute ϕ and δt again with the cross-correlation method (Fukao 1984; Bowman & Ando 1987; Smith *et al.* 2001). For this method, we solve for the maximum cross-correlation coefficient over rotations (0° – 175°) and time-shifts (± 3 s) between the two split waves. We use the previously determined optimum window position for the calculation. However, since the optimal window lengths determined are preferentially short due to possible interference with subsequent phases (Teaby 2005), we also repeat the cross-correlation analysis with 3 s added to the end of the window. Fig. 3 shows the cross-correlation solution of -60° and 0.5 s for one waveform, which is essentially identical (at these periods) to the covariance matrix solution of -59° and 0.487 s. Fig. 4 shows the automatic windowing scheme for the same waveform.

After processing each waveform with the above methods, we manually assign grades of A, B, C, D and NULL to the covariance matrix solution and both cross-correlation solutions based on the signal-to-noise ratio, particle motion analysis, waveform clarity, correlation coefficient or energy contours, and cluster identification match to error contours (see Fig. 4 and Teaby *et al.* 2004). In this case, although the optimum automatic window appears short (Fig. 3), the result is stable over more than 50 per cent of the analysis

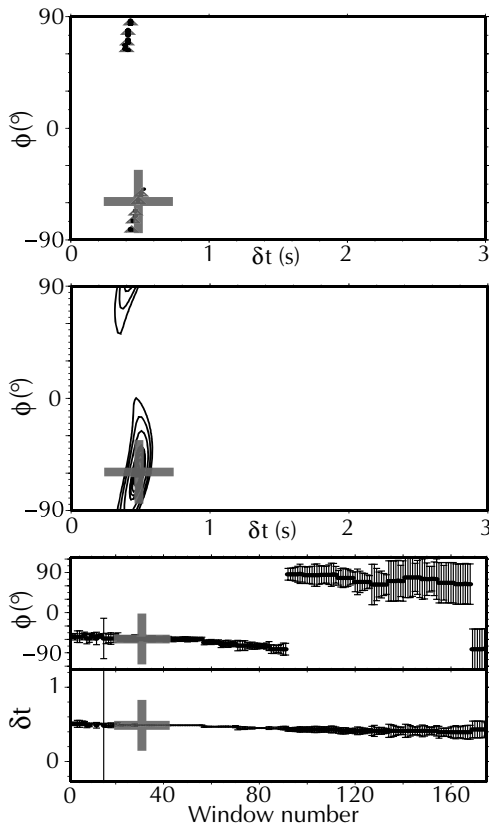


Figure 4. Windowing scheme and clustering method for the waveform solution shown in Fig. 3. In all panels, the optimal solution is shown with the red cross. Top: clusters of all 175 ϕ and δt solutions. Middle: error surface for covariance matrix solution. Note that the error contours are representative of the cluster plot. Bottom: ϕ and δt solutions for each window in the AUTOWIN regime. Note that the optimal solution (red cross) is where the minimal errors occur over the longest range of windows.

windows (Fig. 4 bottom) and is considered a robust solution (Teanby *et al.* 2004). The cross-correlation method usually required a longer analysis window, in agreement with Teanby (2005). The application of both splitting methods also ensured accurate identification of null splitting results (see Wüstefeld & Bokelmann in review), which occur when the shear waves appear to be unsplit. This would arise in the absence of anisotropy along the ray path or because the natural polarization is nearly aligned with the fast or slow orientation. The two analysis methods give a different pattern of splitting results when analysing a null measurement. For an unsplit shear wave, the cross-correlation δt will be less than 0.1 s and ϕ will be 45° off of the initial polarization angle, while the covariance matrix δt will be either large (3 s) or small (<0.1 s) and ϕ will be 0° or 90° off of the initial polarization.

The application of multiple filters sometimes resulted in more than one quality-A solution per waveform. When more than one filter for a given waveform produced a quality-A result, we systematically chose the 0.3–0.7 Hz bandwidth filter consistent with the dominant frequency of most *S* arrivals. Overall, we computed splitting parameters for 1908 waveforms (1304 event-station pairs). After selecting from multiple filters when appropriate, we found 308 quality-A cross-correlation measurements and 268 quality-A covariance matrix measurements recorded at 48 different stations (see Results column in Table 1 for stations with some measurements but no quality-A results).

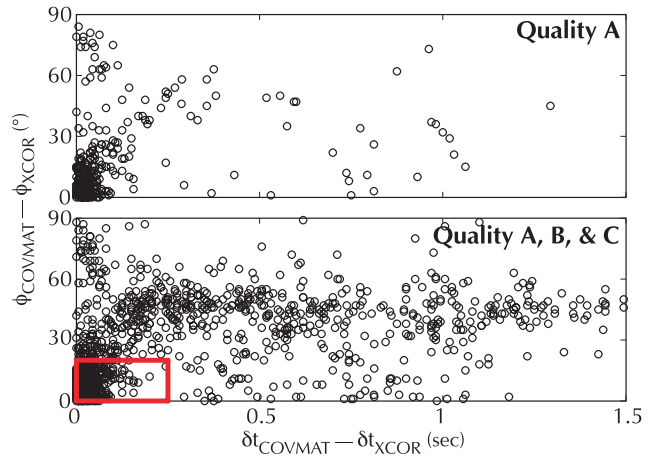


Figure 5. Differences between covariance matrix (COVMAT) and cross-correlation (XCOR) solutions. Top: difference of ϕ_{COVMAT} and ϕ_{XCOR} versus δt_{COVMAT} and δt_{XCOR} for quality A cross-correlation results. Bottom: Similar to top panel, but for quality A, B and C results. Red box encloses null measurements with $<20^\circ$ and <0.25 s difference. Null measurements typically have a 45° difference between the two methods.

Processing each waveform with two different methods yields some inconsistent results. Individually, 194 measurements have consistent cross-correlation and covariance matrix results within $<20^\circ$ similarity in ϕ and <0.25 s difference in δt (Fig. 5). Although the overall splitting patterns of these results are similar to hand-picked quality-A results, we thoroughly investigate any user-bias on manual grading. The median difference between the 308 quality-A cross-correlation results and corresponding covariance matrix measurements is 11° and 0.04 s. Similar splitting patterns are obtained when comparing hand-picked quality-A cross-correlation solutions to those with correlation coefficient >0.75 and to solutions with excellent agreement between the two methods ($<10^\circ$ similarity in ϕ and <0.25 s difference in δt). However, nearly 30 per cent of quality-A cross-correlation results have corresponding covariance matrix results of quality-D or null (Fig. 5). Since all tests show that hand-picked quality-A cross-correlation results are robust and provide the largest number of measurements, we henceforth report only quality-A cross-correlation results. This observation of fewer usable covariance matrix solutions than cross-correlation solutions for noisy data has been reported previously (Restivo & Helffrich 1999; Long & van der Hilst 2005a).

2.4 Spatial averaging

One difficulty with the interpretation of shear wave splitting measurements is that the observed splitting can theoretically occur at any location along the ray path. For complex anisotropy, inadequate interpretation of the results may arise when plotting the splitting measurement at the station or event location or at the epicentral midpoint. Although shear wave splitting tomography based on the Christoffel equation is a possibility (Abt *et al.* 2006), the number of crossing rays in this region is insufficient to obtain a well-constrained result. Therefore, we employ a spatial averaging technique after the method of Audoin *et al.* (2004) to help characterize the overall anisotropy for regions of high complexity.

In this method, we associate each observation with the spatial volume sampled by the ray path and average the splitting results from all the ray paths sampling a given region. In practice, we assign the

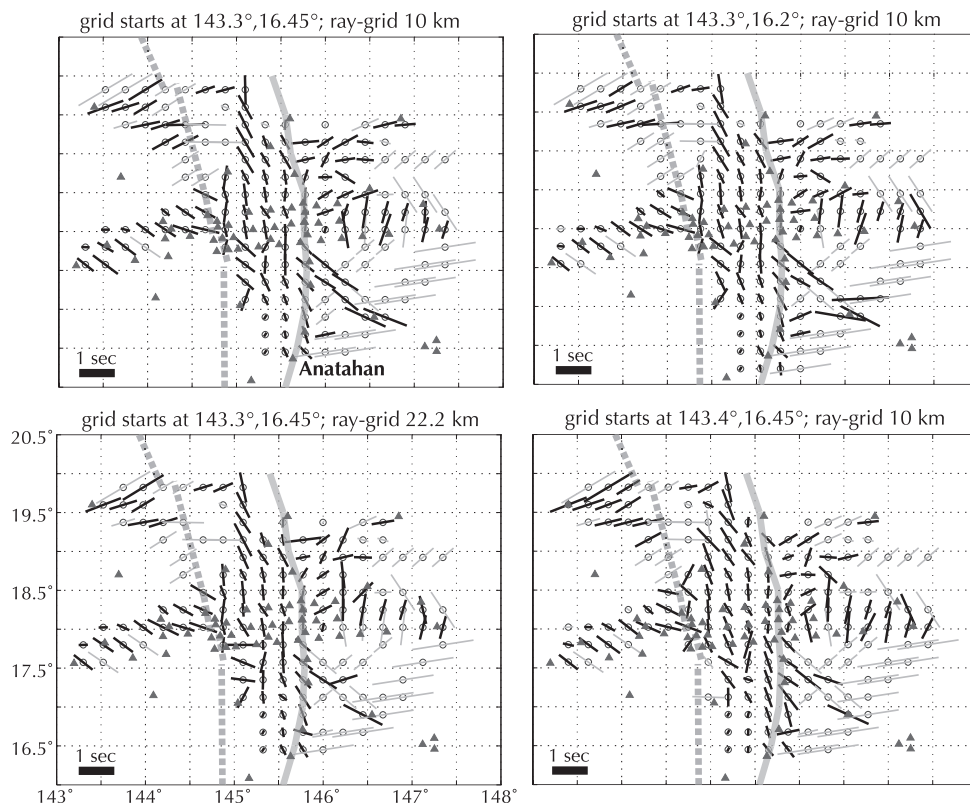


Figure 6. Variations in spatial averaging parameters. Each panel title refers to the starting location of the ‘global grid’ and the ‘ray grid’ spacing. Each panel has identical ‘global grid’ spacing of 25 km. Axes detailed in lower left panel are identical for other three panels. Thick dashed and solid grey lines show location of backarc spreading centre and volcanic arc, respectively. Grey vectors are based on one measurement.

best-fitting cross-correlation splitting parameters to a set of nodes on a circular grid of concentric rings surrounding (and oriented perpendicular to) each ray path. These nodes define the region sampled by the ray path and are henceforth referred to as the ‘ray path grid’. In order to spatially average the splitting parameters from all the individual ray paths, we subsequently superimpose a less-dense global coordinate grid (henceforth referred to as the ‘global grid’). This global grid is oriented parallel to the geographic boundaries of our study area and is equally discretized in each of the X , Y , and Z directions. For each node of the global grid, we calculate the weighted average of all ϕ 's and δt 's from all the ray path nodes that reside within a box centred on the global coordinate node. Averages are computed at the surface global coordinate node ($Z = 0$ km) for all ray path segments shallower than 250 km (see Audoine *et al.* 2004 for details). Inverse distance weighting for each ray path node ensures that splitting parameters from longer ray paths will have smaller influence on many individual global nodes and shorter ray paths have larger influence on a lesser number of global nodes.

Averages are computed only for the northern part of the island arc, where we have the densest ray path coverage. However, we include ray paths from northern earthquakes to southern stations and from southern earthquakes to northern stations if they traverse the averaging region. The averaging scheme breaks down in areas of poor ray path coverage. Therefore, we de-emphasize any results based on single measurements (grey vectors in Fig. 6).

We performed several tests to ensure that the averaging results are robust with respect to the particular choice of averaging parameters. The only free parameters in the averaging scheme are the ‘ray path grid’ node spacing, ‘global grid’ node spacing, and starting location

of the ‘global grid’. Variations of the ‘global grid’ node spacing between 14 and 40 km showed some difference in individual average fast orientations, but the overall pattern remained the same. Averaging results were very similar when varying the ‘ray path grid’ node spacing (left column, Fig. 6). Similarly, varying the starting location of the ‘global grid’ altered individual averaged fast orientations (right column, Fig. 6), but again the overall pattern remained the same. After several trials, we found a ‘ray path grid’ spacing of 10 km and an overlying ‘global grid’ spacing of 25 km to provide the visual best match of averaged results to the raw splitting results. However, throughout the free parameter variations, we emphasize the small change of averaged splitting orientations and magnitudes in regions with a high density of crossing ray paths.

3 RESULTS

3.1 Northern region

Rose diagrams of all quality-A fast orientations plotted at each station show several trends (Fig. 7). The dominant fast splitting orientation is arc-parallel for most stations in the arc and for stations between the arc and backarc spreading centre, whereas the pattern becomes more arc-perpendicular in the far backarc region. We subset individual quality-A splitting results by event depth and plot them at their midpoint to provide further clarity. Results from earthquakes shallower than 250 km (Fig. 8) show roughly arc-parallel splitting orientations for ray paths between the island arc and spreading centre. Most measurements at the OBSs immediately north of Pagan are slightly oblique to arc-parallel with a few arc-perpendicular

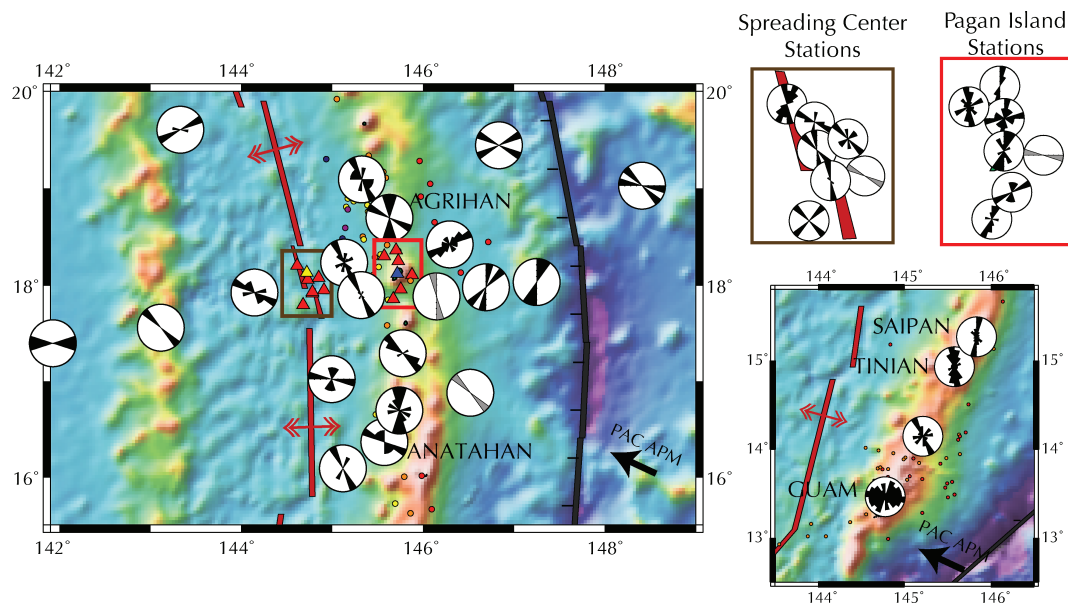


Figure 7. Rose diagrams of all quality-A fast orientations (for all event depths) plotted at each station. All measurements are grouped within azimuth bins of 15° . Grey rose diagrams indicate stations with only one measurement. Dense station clusters are shown in inset panels. Refer to Fig. 1 for base figure explanation.

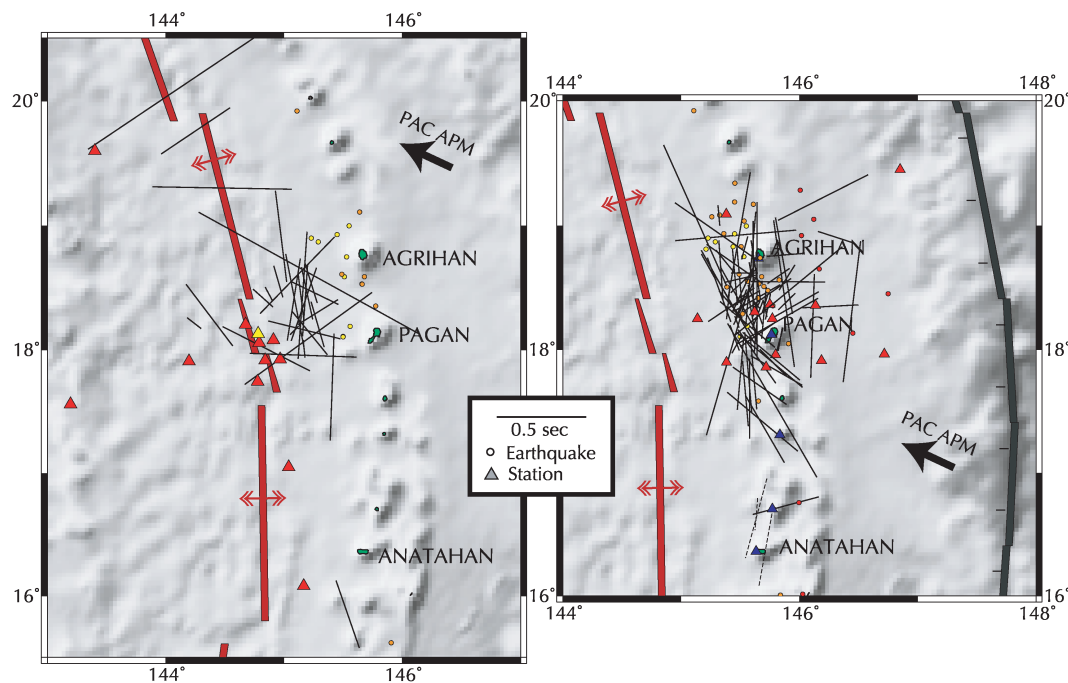


Figure 8. Northern results for events with <250 km hypocentral depth recorded at the stations shown in each panel. Splitting measurements are plotted as lines centred on the epicentral midpoint, oriented by ϕ , and scaled to δt . Dashed lines represent splitting measurements recorded at stations south of Anatahan. Refer to Fig. 1 for further base figure explanation (bathymetry is greyscale version of colour in Fig. 1).

measurements. Mid-latitude island arc stations (Anatahan through Guguan) show variable ϕ ranging between subparallel to APM and subparallel to the arc (Figs 7 and 8). West of the spreading centre and on the West Mariana Ridge, fast orientations are roughly parallel to APM. Shallow event results recorded at stations along the spreading centre show principally arc-parallel fast orientations near the main OBS line. OBSs near the northern part of the spreading centre show fast orientations roughly parallel to the spreading orien-

tation. OBSs in the forearc show variable fast orientations ranging from arc-parallel to very oblique.

Events deeper than 250 km (Fig. 9) show somewhat different patterns compared to shallower events. Fast orientations are subparallel to APM along most of the arc, except at Pagan, where ϕ is subparallel to the arc. Stations at the spreading centre exhibit variable fast orientations, ranging from arc-parallel, APM-parallel, and APM-perpendicular. Stations in the forearc record ϕ subparallel to the arc

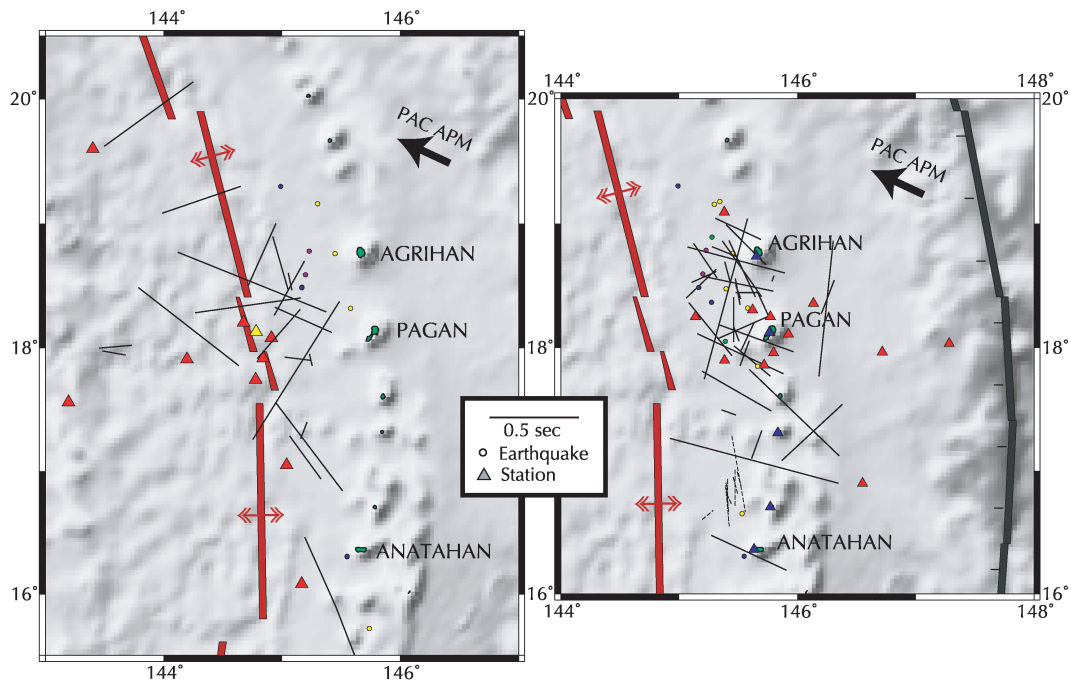


Figure 9. Northern results for events deeper than 250 km recorded at the stations shown in each panel. See Fig. 8 caption.

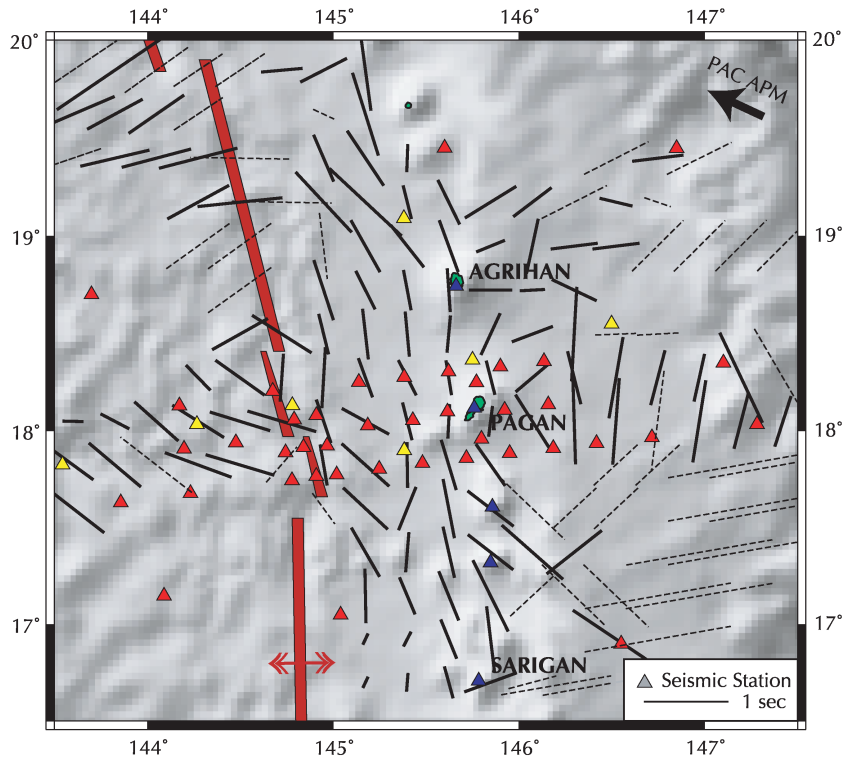


Figure 10. Spatial averaging results for 0–250 km. Results are plotted as lines oriented in the orientation of average ϕ , scaled to average $\delta\tau$, and centred on the system grid nodes. Dashed lines are based on one measurement or are too close to edges of averaging area for meaningful interpretation. See text for discussion and Fig. 1 for base figure explanation.

and stations near the West Mariana Ridge show APM-parallel fast orientations, similar to the orientations found for shallower events.

Spatial averages for the depth range 0–250 km show roughly arc-parallel fast orientations in the island arc and east of the backarc spreading centre (Fig. 10). We observe APM-subparallel ϕ near

the spreading centre and towards the West Mariana Ridge. Some indication of fast orientations subparallel to APM is detected at mid-latitude island arc regions and the northernmost forearc region. These patterns clearly elucidate trends observed in the raw data (Figs 7–9).

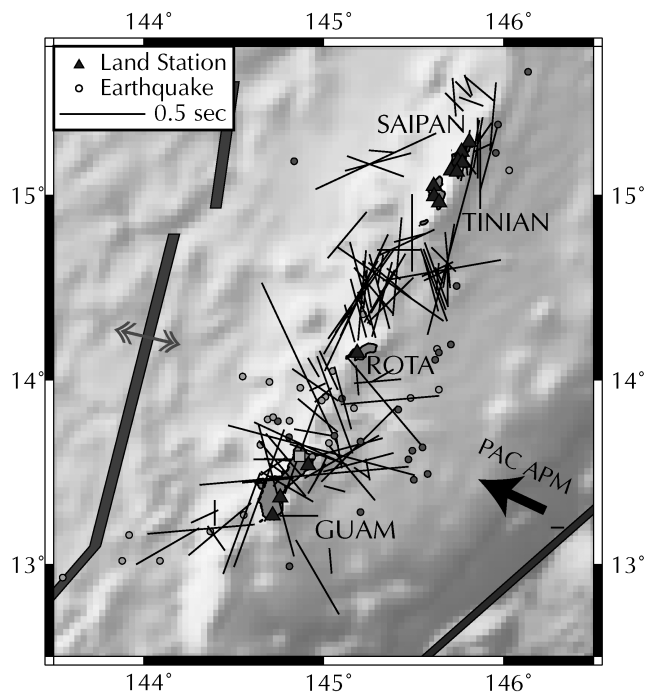


Figure 11. Splitting results for results recorded at all southern stations are plotted at the event-station midpoint, oriented by ϕ , and scaled to δt . Refer to Fig. 8 for base figure explanation.

3.2 Southern region

Nearly all measurements in the southern region have focal depths <250 km and two patterns of fast orientations predominate (Figs 11 and 12). Between Rota and Saipan, we record splitting measurements subparallel and oblique to the arc. In this region, the strike of the arc is $\sim 20^\circ$ and the average ϕ of these measurements is 3.1° . We observe variable splitting orientations near Guam, but can make several general observations from the splitting map (Fig. 12). For example, events in the forearc show variable split-

ting orientations, events north of the island show fast orientations subparallel to APM, and events southwest of the island show dominantly arc-parallel orientations. However, results are complicated and data coverage is sparse.

3.3 Depth extent of anisotropy

We investigate the possibility of depth-dependent lag times, as would be expected if anisotropy extends throughout the depth range studied, and has been noted for several other subduction zones (Yang *et al.* 1995; Fouch & Fischer 1996). Delay times throughout the northern region range from 0.1 to 2.1 s for focal depths <250 km and from 0.1 to 1.5 s for events ≥ 250 km. For both depth ranges, average lag times are 0.55–0.56 s. Southern region delay times range from 0.1 to 1.2 s with a 0.36 s average. There is a lack of systematic variation of δt with hypocentral depth (Fig. 13, right). However, there is a slight suggestion of a small increase of δt with path length that is more apparent for the southern stations (Fig. 13, lower left), but also noticeable at northern stations (upper left).

Percent anisotropy (k) is calculated for the i th ray path by

$$k_i = \frac{\delta t_i V_S}{d_i},$$

where V_S is an assumed S velocity of 4 km s^{-1} and d is the hypocentral distance. Arithmetic mean k_{AVE} and individual k_{MAX} are detailed in Table 2. Mean percent anisotropy for northern and southern events is 1.0 and 1.4 per cent, respectively. Nearly all southern events are between 80 and 200 km, therefore, we cannot discuss the depth extent of anisotropy there, except to mention that the mean value of 1.4 per cent must be characteristic of the upper 80–100 km. For the northern region, mean anisotropy for events shallower than 250 km is 1.3 per cent, which reduces to 0.5 per cent for events 250–600 km depth. The reduction in average anisotropy with depth is consistent with a small amount azimuthal anisotropy below 250–300 km in the mantle wedge (Fischer & Wiens 1996). We note that, since there is little or no variation in splitting time with depth or path length, the maximum percent anisotropy can be calculated with the minimum path length, which gives a maximum percent anisotropy of 1.6 per cent, which is slightly higher than the mean calculations.

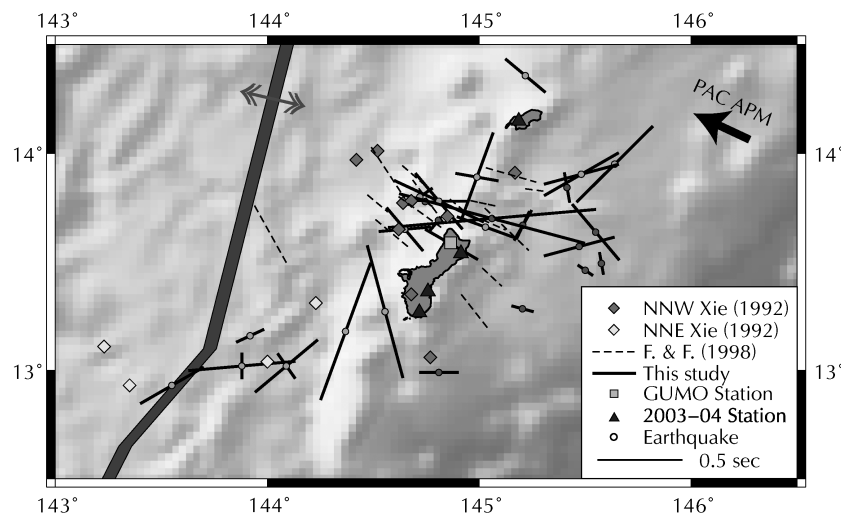


Figure 12. Comparison of results near Guam. All splitting results are plotted at the epicentre, oriented by ϕ , and scaled to δt . Solid black lines are results from this study and dashed lines are local S results from Fouch & Fischer (1998). Diamonds show qualitative NW (pink) or NE (yellow) fast orientations from Xie (1992). Circles are events used in this study. See text for discussion and Fig. 1 for base figure explanation.

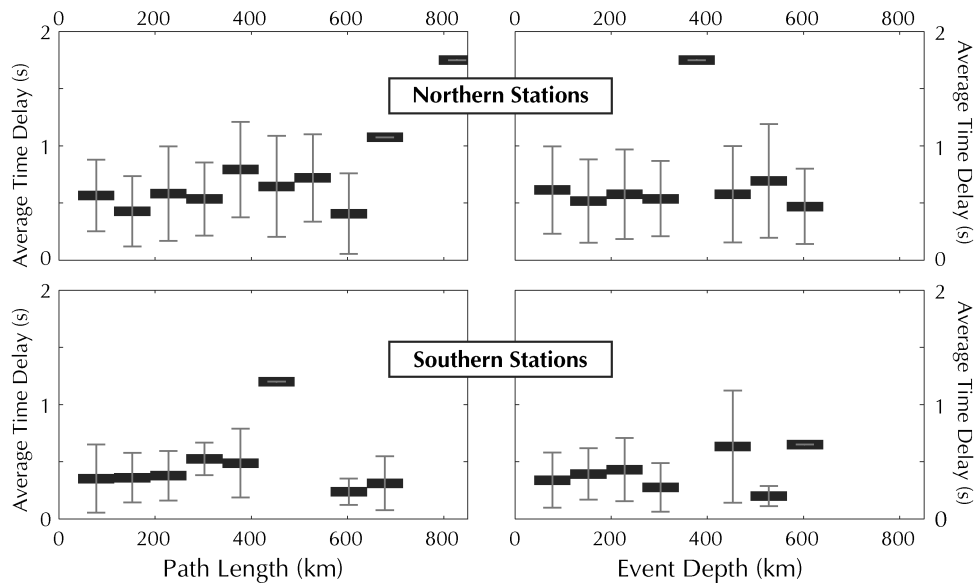


Figure 13. Variation of mean time delay versus path length (left) and event depth (right) for northern (latitude $> 16^\circ\text{N}$) (top panel) and southern (bottom panel) stations. Bars span the 75-km width for each mean δt . Trends are independent of bin width. Note that the long path lengths and deep events at the southern stations are from earthquakes in the northern region.

Table 2. Percent anisotropy calculations assuming $V_S = 4 \text{ km s}^{-1}$. Northern and southern event subsets refer to events north and south of 16°N , respectively. See text for discussion.

Event subset	Depth range (km)	K_{AVE} (per cent)	k_{MAX} (per cent)
All	All	0.9	5.7
All	<250	1.3	5.7
All	≥ 250	0.4	2.0
Northern	All	0.7	5.7
Northern	<250	1.2	5.7
Northern	≥ 250	0.4	1.8
Southern	All	1.4	5.5

4 DISCUSSION

4.1 Comparison with other observations

4.1.1 Prior Mariana studies

Shear wave splitting fast orientations parallel to APM recorded at the GUMO GSN station on Guam are commonly cited as evidence for a corner flow dominant mantle flow regime. Previously reported fast splitting orientations at Guam range from -20° to -80° . With splitting times of less than $\sim 0.4 \text{ s}$ (Fouch & Fischer 1998; Fig. 12). Xie (1992) also observed $\delta t < 0.4 \text{ s}$ and NNW–SSE fast orientations for events near Guam. The earlier GUMO study additionally found NNE–SSW ϕ for events southwest of the island. Fast orientations in this study from events southwest of Guam are roughly arc-parallel (Fig. 12), in agreement with the comparable qualitative measurements of Xie (1992) (yellow diamonds in Fig. 12); the later GUMO study did not report measurements from earthquakes in this area. Events located closer to the island show predominantly APM-subparallel fast orientations for all three studies and events in the forearc have variable orientations. Fig. 12 shows agreement of all Guam splitting measurements, with fast orientations dependent on earthquake location, such that the dominant pattern is of APM-parallel ϕ near the island and arc-parallel ϕ southwest of the island.

Fouch & Fischer (1998) calculated percent anisotropy finding values between 0.65 and 2.25 per cent. Approximate calculations from this study indicate similar percent anisotropy of 1.4 per cent for southern events.

A more recent OBS study by Volti *et al.* (2006), using three of the same 2001–2002 OBS records used in this study and three OBSs from an earlier 1999–2000 deployment, found fast orientations subparallel to APM in the northernmost part of the arc and along the West Mariana Ridge and ϕ quasi-perpendicular to the trough axis near the spreading centre. We image fast orientations subparallel to APM on the West Mariana Ridge and to the west of the Mariana spreading centre in agreement with the previous OBS study. At the same time, our larger aperture array with greater station density allows us to image the rotation of fast orientations into the arc-parallel orientation at the backarc spreading centre, which was not observed in the previous studies.

In addition to shear wave splitting and seismic anisotropy investigations, other studies suggest preliminary interpretations about mantle flow patterns. Preliminary velocity and attenuation tomography results from the 2003–2004 deployment show separate low velocity and high attenuation regions beneath the volcanic arc and backarc spreading centre (Barklage *et al.* 2006; Pozgay *et al.* 2006). A small higher velocity and lower attenuation region separates these two zones at shallow depth ($\lesssim 50 \text{ km}$). This region might represent the boundary between different flow mechanisms—arc-parallel flow surrounding the island arc and APM-parallel flow beyond the backarc spreading centre. In addition, detailed geochemical analyses of the Mariana arc and trough suggest arc-parallel mantle flow between several centres of passive upwelling directly beneath the spreading centre (Pearce *et al.* 2005).

4.1.2 Other subduction zones

Several other subduction zones exhibit varying fast orientations that can be compared to observations in the Marianas. In Tonga, percent anisotropy is estimated at ~ 1.5 per cent for the upper $\sim 200 \text{ km}$

(Fischer & Wiens 1996), similar to calculations in this study, and fast orientations at stations near the arc are arc-parallel, while APM-parallel values are observed farther into the backarc near the Fiji plateau (Bowman & Ando 1987; Smith *et al.* 2001). Southward infiltration of the Samoan plume above the retreating Pacific slab is one likely interpretation for this pattern, in agreement with geochemical evidence for plume infiltration (Turner & Hawkesworth 1998). Our observations in the Mariana arc show a similar pattern of arc-parallel fast orientations near the arc and APM-parallel ϕ in the far backarc. In both subduction zones, the rotation from arc-parallel to APM-parallel occurs near the backarc spreading centre. The Mariana region does not show a slab window or the slab rollback thought to contribute to the Tonga dynamics, however the similarity of shear wave splitting measurements in the two different subduction zones may be indicative of a general pattern of upper-mantle flow in arcs with active backarc spreading.

Local S splitting results in Kamchatka show a maximum of 2.6 per cent anisotropy and highly variable fast splitting orientations (Levin *et al.* 2004). Fast orientations behind the arc are roughly arc-parallel throughout the study area. However, the northeastern region shows oblique and scattered ϕ near the trench and arc, compared to relatively uniform arc-perpendicular ϕ in the southwest. Levin *et al.* (2004) conclude that corner flow is highly localized near the southern region and suggest that complex slab morphology and temporal slab dip variations might explain the heterogeneous fast orientations in the north. In our study, we also observe highly variable splitting orientations and time lags in some regions and observe similar percent anisotropy. However, we observe nearly opposite fast orientations compared to Kamchatka, with arc-parallel fast orientations dominating near the Mariana arc, but APM-parallel ϕ in the far backarc.

Splitting orientations from teleseismic S phases recorded in southern Japan are dominantly trench-parallel at the arc and trench-perpendicular in the backarc (Long & van der Hilst 2005b), while local S observations in central Honshu and Hokkaido show arc-parallel fast orientations in the forearc and APM-parallel ϕ beneath the arc (Nakajima & Hasegawa 2004; Long & van der Hilst 2005b). Fast orientations in the northern part of the Izu arc are oriented subparallel to both the convergence direction and the trench-parallel orientation (Anglin & Fouch 2005), whereas ϕ is consistently trench-parallel in the Ryukyu arc (Long & van der Hilst 2006). Fast orientations in this study are similar to that observed throughout parts of Japan and the Izu and Ryukyu islands and our estimate of percent anisotropy for northern events agrees well with similar calculations in Japan (Fouch & Fischer 1996).

In addition to those mentioned above, other subduction zones are also dominated by arc-parallel fast splitting orientations with some nearby APM-parallel component. Fast splitting orientations in the mid-latitude regions of the South American subduction zone are dominantly trench-parallel in regions of 'normal' slab behaviour and are subparallel to the strike of slab contours in regions where the slab flattens (Anderson *et al.* in review). Fast orientations are dominantly trench-parallel throughout the Central American arc and backarc and are only trench-perpendicular in the forearc (Abt *et al.* 2006), whereas the north island of New Zealand shows trench-parallel ϕ in the arc and forearc with trench-perpendicular ϕ only in the backarc (Marson-Pidgeon *et al.* 1999; Audoine *et al.* 2004; Styles *et al.* 2006). Geodynamic modelling results typically suggest APM-parallel mantle flow, however most arcs show arc-parallel fast orientations implying arc-parallel mantle flow. This study shows that although APM-parallel fast orientations are present in the far backarc and in a small region surrounding the island of Guam, arc-

parallel fast splitting orientations predominate throughout the Mariana subduction system.

4.2 Possible factors controlling seismic anisotropy in the Mariana Arc

4.2.1 Fossil anisotropy in the subducting slab

Anisotropy might be controlled by fossil sea floor spreading (FSS) (Hess 1964) from ray paths travelling through the slab. Based on 45° magnetic isochrons prior to subduction (Nakanishi *et al.* 1992), slab dips of ~88° and ~55°, and arc strikes of ~0° and ~20° for the northern and southern regions, respectively, and assuming the dominant fast anisotropy orientation in the oceanic lithosphere is isochron-perpendicular (Forsyth 1992), we would expect fast orientations approximately N–S or NNW–SSE in the northern region and roughly –20° in the south. Although anisotropy in the slab could be distinguished by time lag differences between events in the upper or lower plane of the double seismic zone (Wiens *et al.* 2005), data for such investigation is insufficient. Similarly, any anisotropy due to in-slab strain resulting from downdip extension or compression is not resolvable with this study.

We can, however, infer the presence or absence of slab anisotropy by other means. Along the arc and east of the trough, arc-parallel ϕ dominates for events <250 km (Figs 7–10). The arc-parallel orientation is similar to the FSS direction in the northern region, however we do not attribute the majority of these measurements to anisotropy in the slab because most ray paths travel primarily through the mantle wedge and sample a minimal region of the slab itself. Several deep northern events recorded at Pagan and at southern stations show fast orientations parallel to predicted FSS orientations with small δt and may result from slab anisotropy (dashed vectors in Fig. 9). These ray paths sample a significant amount of the slab and the solutions are oriented in the expected FSS directions and are in agreement with prior slab anisotropy solutions with average lag times of ~0.25 s (Volti *et al.* 2006). APM-parallel fast orientations are recorded at Agrihan and Guguan.

4.2.2 Anisotropy in the crust

Considering the apparent lack of depth dependence on our splitting measurements, crustal anisotropy might seem a plausible source. However, we first note that most crustal anisotropy measurement are on the order of 0.05–0.2 s (Savage 1999), which is much smaller than our delay times (average δt is ~0.5 s). Second, we note that crustal thickness beneath the Mariana Trough is only ~5–7, ~20 km thick beneath island arc stations, and ~10 km thick beneath forearc stations (Takahashi *et al.* 2007). If the crust was the main source of anisotropy at OBS stations, where we observe an average 0.5 s delay time, percent anisotropy would be on the order of >28 per cent (based on 10 km thick crust and shear velocity of 4 km s⁻¹), which is significantly larger than has been observed in crustal rocks (Babuska & Cara 1991; Crampin 1994). Although we cannot completely rule out a small effect of crustal anisotropy on our measurements, it cannot be a major source of splitting in our measurements.

4.2.3 Effect of water on the anisotropic slip system

Significant amounts of water and high shear stress may align the olivine a -axis perpendicular to the direction of maximum strain, resulting in a shear wave splitting fast orientation perpendicular

to mantle flow (Jung & Karato 2001). Recent modelling results show that such changes in olivine slip systems are likely for slow subduction rates ($< \sim 3\text{--}4$ cm/yr) and in areas with extremely high stresses ($\gtrsim 50$ MPa), low temperatures (700–1000 °C), and presence of water, for example in forearcs (Kneller *et al.* 2005). Geodynamic modelling (Currie & Hyndman 2006) and heat flow (Blackwell *et al.* 1982) results suggest that the upper mantle beneath arc and backarc regions is characterized by temperatures that are too high (> 1200 °C) to produce this alignment. Thus, ‘B-type fabric’ is not a good explanation for the extensive region of along-strike fast orientations extending from the arc to the backarc spreading centre in our results.

B-type fabric remains a possibility for the interpretation of forearc measurements, where the mantle is cold and has a high water content, as indicated by widespread serpentinization (Fryer 1996). However, if B-type fabric exists in the Mariana forearc, we would expect a small magnitude of anisotropy and the arc-parallel ϕ measurements would be interpreted as APM-parallel flow. Since island arc fast orientations are predominantly arc-parallel and that area is too hot for B-type fabric, this scenario would then require different physical mechanisms to invoke APM-parallel flow beneath the forearc and arc-parallel flow beneath the arc. However, due to the predominance of arc-parallel ϕ throughout much of the arc system and the significant magnitude of splitting observed in this region, we suggest that the forearc fast orientations are probably due to similar mechanisms that produce the arc-parallel fast orientations beneath the arc and are probably not due to B-type fabric.

4.2.4 Oriented melt pockets

Experimental studies show that a small amount of melt can weaken the overall *a*-axis alignment, such that abundant melt bands aligned in the direction of stress would rotate the *a*-axis 90° to the dominant flow direction (Holtzman *et al.* 2003). If the flow direction in the vicinity of the backarc spreading centre were parallel to the spreading direction as inferred from *a*-axis orientations obtained by ocean-bottom electromagnetic studies (Baba *et al.* 2004), we would expect fast orientations aligned 90° to the extension direction. We observe fast orientations that are dominantly ridge-parallel near the arc and switch to ridge-perpendicular immediately to the west of the spreading centre axis (Figs 7–10). This might suggest dominantly ridge-perpendicular mantle flow along the entire spreading centre with the along-strike fast orientation between the arc and spreading centre produced by aligned melt bands.

Although this hypothesis requires further study, there are several difficulties. This model would warrant significant melt porosity in the upper mantle over a wide depth range and over a large spatial extent; it is not clear whether sufficient *in situ* melt exists in the upper mantle to cause this effect on a wide scale. In fact, *U*-series disequilibria studies suggest that the porosity of the upper mantle is very low, both beneath oceanic spreading centres (Spiegelman & Elliott 1993; Lundstrom *et al.* 1998) and island arcs (Turner & Foden 2001). In addition, if widespread melt exists beneath the arc and between the arc and backarc spreading centre where we see along-strike fast orientations, it is not clear why this mechanism would not also operate somewhat west of the spreading centre where we see APM-parallel fast orientations.

4.2.5 Slab-driven flow

A long-standing model for mantle flow in a subduction zone consists of mantle wedge material coupled to the downgoing slab producing

APM-parallel fast orientations (e.g. van Keken 2003). The Mariana arc is often cited as a model for APM-parallel corner flow. However, we observe APM-parallel fast orientations only for deep events, at stations near the West Mariana Ridge, and close to Guam. We record a slight rotation of fast orientations towards APM-parallel at mid-latitude island arc stations, but fast orientations are dominantly arc-parallel. We conclude that APM-parallel corner flow is likely at $\gtrsim 250$ km distance and depth away from the trench, but is not dominant throughout the arc system.

4.2.6 Arc-parallel mantle flow due to slab morphology and convergence angle variations

One mechanism that may be important for producing arc-parallel flow in the Mariana wedge is arc-parallel flow in the asthenosphere. Pressure gradients that drive flow may be generated in a variety of ways, such as flow through slab tears or windows due to spatial (Smith *et al.* 2001) or temporal variations (Levin *et al.* 2004), slab rollback (Russo & Silver 1994; Buttles & Olson 1998), variations in downgoing slab morphology (Hall *et al.* 2000), or variations in convergence angle along-strike of the arc (Honda & Yoshida 2005).

Analytical models show that a change in slab dip of one degree over ~ 100 km of along-strike distance will produce arc-parallel pressure gradients in the wedge corner that may, in turn, elicit arc-parallel flow above the slab (Hall *et al.* 2000). Numerical modelling results based on this suggest that the magnitude of arc-parallel flow must be > 25 per cent of the plate convergence rate to noticeably rotate olivine *a*-axes away from an APM orientation (Blackman & Kendall 2002). Such arc-parallel flow would decrease in magnitude with distance away from the wedge corner. In the Marianas, slab dip decreases by $\sim 40^\circ$ between Agrihan and Guam, a distance of ~ 555 km. In accordance with modelling results of Hall *et al.* (2000), we would expect arc-parallel flow near the wedge corner resulting from large changes in slab dip and waning effects of arc-parallel flow with increasing distance away from the corner. Such a model is consistent with our observations of arc-parallel ϕ east of the spreading centre for events shallower than ~ 250 km and APM-parallel ϕ for deeper events and at stations west of the spreading centre. If arc-parallel flow is due to slab dip variations, effects may only be imaged near the arc for shallow events (< 250 km) with waning influence to the spreading centre ($\sim 250\text{--}300$ km laterally). Additionally, laboratory experimental results modelling a steeply dipping slab suggest that *a*-axis alignment may only predominate near the slab (Buttles & Olson 1998), further reinforcing a confined spatial extent of arc-parallel flow.

4.2.7 Arc-parallel pressure gradients—geodynamic modelling

To illustrate the qualitative viability of arc-parallel pressure gradients controlling the LPO structure within the mantle wedge, we create a 2-D finite-element model of mantle wedge flow using a stress- and temperature-dependent viscosity structure. First, we calculate the viscosity structure of the mantle wedge, with the known inverse exponential relationship to temperature (Karato & Wu 1993), using prior thermal modelling methods (Conder *et al.* 2002; Conder 2005). The viscosities are lowest just outside of the ‘cold nose’ forearc, in the uppermost corner where temperatures and corner flow strain rates are highest. We impose an arc-parallel pressure gradient of a few kPa km⁻¹ to that resultant viscosity structure and calculate the induced arc-parallel velocity structure (Fig. 14a) and the subsequent strain rate from the induced flow (Fig. 14b). The pressure gradient

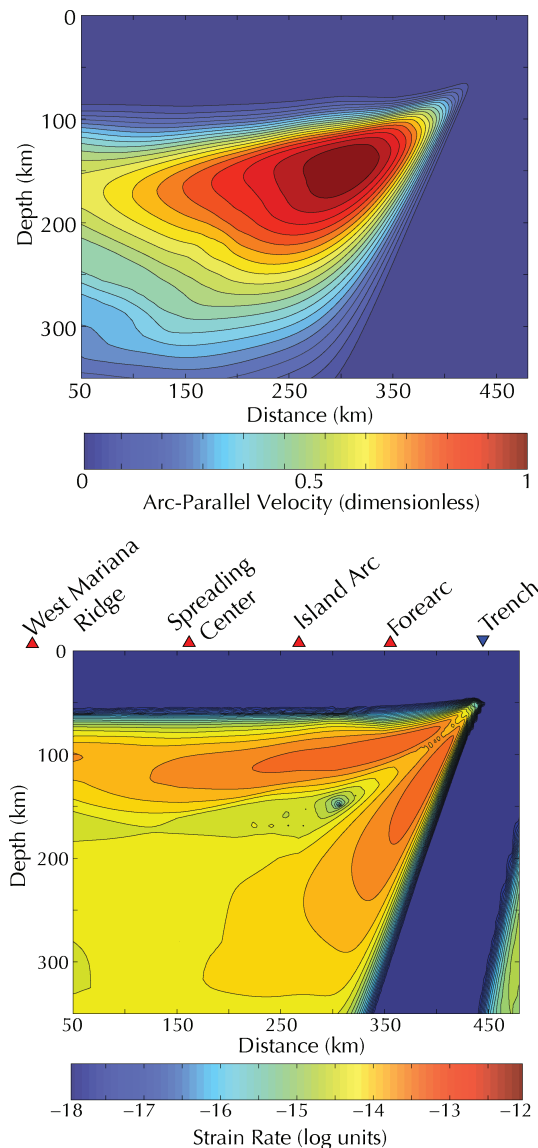


Figure 14. Arc-parallel mantle flow velocity in dimensionless units (a) and resulting strain rate in log units (b) from applying an along-strike pressure gradient to the 2-D variable viscosity, non-Newtonian flow models patterned after the northern Mariana mantle wedge. Note that strain rates far away from the wedge corner are overestimated. See text for discussion.

is an *a priori* assumption in this simple modelling, the purpose of which is to investigate whether a pressure gradient can produce the observed spatial distribution of splitting orientations. Thus, the magnitude of both the pressures and the flow velocity are meant to be representative and should not be as a precise measure.

We approximate conditions for a cross-section along our main OBS line near Pagan in our model with a slab dip of $\sim 75^\circ$ and a convergence rate of 4 cm yr^{-1} . To keep the methodology simple, we ignore the spreading centre in these models. While pressure gradients for either flow through slab tears or pressure-gradients from changes in slab morphology will be strongest near the corner, our 2.5-D assumption requires a constant pressure gradient over the entire wedge, noting that a variable pressure gradient would be possible with full 3-D modelling, but is outside the scope of this paper for our illustrative purposes. As such, arc-parallel flow rates far from the corner are likely overestimated relative to the

arc-parallel flow rates within the corner. However, even with this overestimation, clear differences are apparent between the backarc and the uppermost corner of the wedge.

Two localized regions of high strain rate are visible in Fig. 14(b). One region is along the top of the slab and extends to depths $\gtrsim 150 \text{ km}$. The other region is just below the overriding Philippine Sea Plate with a maximum depth extent of $\sim 150 \text{ km}$ and dissipates towards the backarc. In this light, the high strain rates in the wedge corner dissipate between the island arc and spreading centre, becoming close to the ambient background. These regions of high strain rate due to arc-parallel velocity gradients illustrate regions of expected contribution to arc-parallel fast orientations and are a good match to our observations. Similarly, 3-D models with curved slabs also show strong trench-parallel stretching in the wedge corner (Kneller & van Keken 2006). Ray paths that travel through these high strain regions result in dominantly arc-parallel fast orientations, whereas ray paths travelling mostly through regions of low arc-parallel strain rate have roughly APM-parallel ϕ . In contrast, deep events recorded at northern island arc stations are nearly all subparallel to APM. Ray paths from deeper hypocentres will spend more time at depths that are largely unaffected by arc-parallel pressure gradients (Fig. 14b), and are more affected by corner flow in a direction parallel to APM.

5 CONCLUSIONS

Local *S* splitting results show complex patterns along and across the Mariana subduction system. Dense seismic arrays, multiple data analysis techniques, and comprehensive manual and numerical grading schemes provide a high-resolution image of seismic anisotropy patterns throughout the region. Shallow and intermediate depth events exhibit predominantly arc-parallel fast orientations in the forearc, island arc and backarc regions. Splitting measurements recorded at stations west of the backarc spreading centre and measurements from deep events show fast orientations subparallel to APM. We observe larger average splitting times in the northern region (0.55 s) compared to the southern region (0.36 s), but there is no increase in lag time with depth. Arc-parallel fast orientations for shallow and intermediate depth events are likely controlled by arc-parallel flow due to trench-parallel pressure gradients induced by a combination of slab dip and convergence angle variations and by arc-parallel extension. These causes would dominate near the wedge corner and have waning influence at greater distances. Our results indicate a transition at the backarc spreading centre from arc-parallel fast orientation on the east side to APM-parallel on the western side, similar to the transition observed in other subduction zones (e.g. Tonga arc). In addition, modelling results suggest that any arc-parallel pressure gradient induced by tectonic variations would not affect the far backarc and we see no evidence of arc-parallel fast orientations in this region. We conclude that simple 2-D corner flow does not dominate throughout the Mariana arc system and the slab–mantle system is only strongly coupled at $\geq \sim 250 \text{ km}$ depth and at large distances from the wedge corner.

ACKNOWLEDGMENTS

Thanks to Gideon Smith, Nick Teanby, and Martha Savage for helpful comments on shear wave splitting methods and implementation. Theodora Volti provided two OBS orientations. Martha Savage, Vadim Levin, Karen Fischer, Megan Anderson, Maureen Long, Garrett Euler, Erica Emry, Moira Pyle and one anonymous reviewer

all provided helpful advice and suggestions that greatly improved this paper. We thank numerous people, particularly Patrick Shore, Spahr Webb, Allan Sauter, Patrick Jonke, Juan Camacho, Joe Kaipat and Ray Chong, as well as the captain and the crew of the R/V Kaiyo, the R/V Wecoma, and the Super Emerald for assistance with deploying and recovering the seismographs. Land seismic instrumentation was provided by the PASSCAL program of the Incorporated Research Institutions in Seismology (IRIS) and the Lamont Ocean Bottom Seismograph Facility provided ocean bottom seismographs. This research was supported by the MARGINS program under National Science Foundation grant OCE0001938.

REFERENCES

- Abt, D.L., Fischer, K.M., Martin, L.J., Abers, G.A., Protti, J.M., Gonzalez, V. & Strauch, W., 2006. Shear-wave splitting tomography in the central American subduction zone: implications for flow and melt in the mantle wedge, *EOS Trans. AGU, Fall Meet. Suppl.*, **87**(52), T22C-05.
- Anderson, M.L., Zandt, G. & Wagner, L., in review. Along-strike mantle flow variations in a segment of the South American subduction zone, Chile and Argentina, *Ear. Planet. Sci. Lett.*, in review.
- Anglin, D.K. & Fouch, M.J., 2005. Seismic anisotropy in the Izu-Bonin subduction system, *Geophys. Res. Lett.*, **32**, doi:10.1029/2005GL022714.
- Audoine, E., Savage, M.K. & Gledhill, K., 2004. Anisotropic structure under a back arc spreading region, the Taupo Volcanic Zone, New Zealand, *J. Geophys. Res.*, **109**(B11305), doi:10.1029/2003JB002932.
- Baba, K., Seama, N., Goto Ichiki, T., Schwalenberg, K., Suyehiro, K. & Utada, H., 2004. Electrical transection of the upper mantle in the Mariana subduction system, *The 17th International Workshop on Electromagnetic Induction in the Earth*, Natl. Geophys. Res. Inst., Hyderabad, India.
- Babuska, V. & Cara, M., 1991. *Seismic Anisotropy in the Earth*, pp. 217, Kluwer Academic Publishers, Dordrecht, The Netherlands.
- Barklage, M.E., Conder, J.A., Wiens, D.A., Shore, P.J., Shiobara, H., Sugioka, H. & Zhang, H., 2006. 3-D seismic tomography of the Mariana mantle wedge from the 2003–2004 passive component of the Mariana subduction factory imaging experiment, *EOS Trans. AGU, Fall Meet. Suppl.*, **87**(52), T23C-0506.
- Blackman, D.K. & Kendall, J.-M., 2002. Seismic anisotropy in the upper mantle 2. Predictions for current plate boundary flow models, *Geochem. Geophys. Geosys.*, **3**(9), 8602, doi:10.1029/2001GC000247.
- Blackwell, D.D., Bowen, R.G., Riccio, J. & Steele, J.L., 1982. Heat flow, arc volcanism, and subduction in Northern Oregon, *J. Geophys. Res.*, **87**, 8735–8754.
- Bowman, J.R. & Ando, M., 1987. Shear-wave splitting in the upper-mantle wedge above the Tonga subduction zone, *Geophys. Jour. Roy. Astr. Soc.*, **88**, 25–41.
- Buttles, J. & Olson, P., 1998. A laboratory model of subduction zone anisotropy, *Ear. Planet. Sci. Lett.*, **164**, 245–262.
- Conder, J.A., 2005. A case for hot slab surface temperatures in numerical viscous flow models of subduction zones with an improved fault zone parameterization, *Phys. Ear. Planet. Int.*, **149**, 155–164, doi:10.1029/j.pepi.2004.09.018.
- Conder, J.A., Wiens, D.A. & Morris, J., 2002. On the decompression melting structure at volcanic arcs and back-arc spreading centers, *Geophys. Res. Lett.*, **29**(15), doi:10.1029/2002GL015390.
- Crampton, S., 1994. The fracture criticality of crustal rocks, *Geophys. J. Int.*, **118**, 428–438.
- Currie, C.A. & Hyndman, R.D., 2006. The thermal structure of subduction zone back arcs, *J. Geophys. Res.*, **111**, B08404, doi:10.1029/2005JB004024.
- Everitt, B., 1993. *Cluster Analysis*, 3rd ed., pp. 170, Halsted Press, London.
- Fischer, K.M. & Wiens, D.A., 1996. The depth distribution of mantle anisotropy beneath the Tonga subduction zone, *Ear. Planet. Sci. Lett.*, **142**, 253–260.
- Fischer, K.M., Parmentier, E.M., Stine, A.R. & Wolf, E.R., 2000. Modeling anisotropy and plate-driven flow in the Tonga subduction zone back arc, *J. Geophys. Res.*, **105**(B7), 16 181–16 191.
- Forsyth, D.W., 1992. Geophysical constraints on mantle flow and melt generation beneath mid-ocean ridges, in *Mantle Flow and Melt Generation at Mid-Ocean Ridges*, 361, eds Phipps Morgan, J., Blackman, D.K. & Sinton, J.M., American Geophysical Union, Washington, D.C.
- Fouch, M.J. & Fischer, K.M., 1996. Mantle anisotropy beneath northwest Pacific subduction zones, *J. Geophys. Res.*, **101**(B7), 15 987–16 002.
- Fouch, M.J. & Fischer, K.M., 1998. Shear wave anisotropy in the Mariana subduction zone, *Geophys. Res. Lett.*, **25**(8), 1221–1224.
- Fryer, P., 1996. Evolution of the Mariana convergent plate margin system, *Rev. Geophys.*, **34**(1), 89–125.
- Fukao, Y., 1984. Evidence from core-reflected shear waves for anisotropy in the Earth's mantle, *Nature*, **309**, 695–698.
- Hall, C., Fischer, K.M., Parmentier, E. & Blackman, D.K., 2000. The influence of plate motions on three-dimensional back arc mantle flow and shear wave splitting, *J. Geophys. Res.*, **105**(B12), 28 009–28 033.
- Hess, H.H., 1964. Seismic anisotropy of the uppermost mantle under oceans, *Nature*, **203**, 629–631.
- Heuret, A. & Lallemand, S., 2005. Plate motions, slab dynamics and back-arc deformation, *Phys. Ear. Planet. Int.*, **149**, 31–51.
- Holtzman, B.K., Kohlstedt, D.L., Zimmerman, M.E., Heidelback, F., Hiraga, T. & Hustoft, J., 2003. Melt segregation and strain partitioning: implications for seismic anisotropy and mantle flow, *Science*, **301**, 1,227–1,230.
- Honda, S. & Yoshida, T., 2005. Effects of oblique subduction on the 3-D pattern of small-scale convection within the mantle wedge, *Geophys. Res. Lett.*, **32**(L13307), 1–4, doi:10.1029/2005GL023106.
- Jung, H. & Karato, S., 2001. Water-induced fabric transitions in olivine, *Science*, **293**, 1,460–1,463.
- Karato, S., 2003. Mapping water content in the upper mantle, in *Inside the Subduction Factory*, 324, ed. Eiler, J., American Geophysical Union, Washington, D.C.
- Karato, S.-I. & Wu, P., 1993. Rheology of the upper mantle: a synthesis, *Science*, **260**(5109), 771–778.
- Kato, T., Beavan, J., Matsushima, T., Kotake, Y., Camacho, J.T. & Nakao, S., 2003. Geodetic evidence of back-arc spreading in the Mariana Trough, *Geophys. Res. Lett.*, **30**(12), 1625–1629.
- Kelley, K.A., Plank, T., Newman, S., Stolper, E.M., Grove, T.L., Parman, S. & Hauri, E., 2003. Mantle melting as a function of water content in arcs, *EOS Trans. AGU, Fall Meet. Suppl.*, **84**(46), Abstract V41D-06.
- Kneller, E.A. & van Keken, P.E., 2006. The effects of 3D slab geometry on deformation in the mantle wedge, *EOS Trans. AGU, Fall Meet. Suppl.*, **87**(52), Abstract T22C-07.
- Kneller, E.A., van Keken, P.E., Karato, S. & Park, J., 2005. B-type olivine fabric in the mantle wedge: Insights from high-resolution non-Newtonian subduction zone models, *Ear. Planet. Sci. Lett.*, **237**, 781–797.
- Levin, V., Droznin, D., Park, J. & Gordeev, E., 2004. Detailed mapping of seismic anisotropy with local shear waves in southeastern Kamchatka, *Geophys. J. Int.*, **158**, 1,009–1,023.
- Long, M.D. & Van Der Hilst, R.D., 2005a. Estimating shear-wave splitting parameters from broadband recordings in Japan: A comparison of three methods, *Bull. Seis. Soc. Am.*, **95**(4), 1346–1358.
- Long, M.D. & Van Der Hilst, R.D., 2005b. Upper mantle anisotropy beneath Japan from shear wave splitting, *Phys. Ear. Planet. Int.*, **151**, 206–222.
- Long, M.D. & Van Der Hilst, R.D., 2006. Shear wave splitting from local events beneath the ryukyu arc: trench-parallel anisotropy in the mantle wedge, *Phys. Ear. Planet. Int.*, **155**(3–4), 300–312.
- Lundstrom, C.C., Williams, Q. & Gill, J., 1998. Investigating solid mantle upwelling rates beneath mid-ocean ridges using U-series disequilibria: I. A global approach, *Ear. Planet. Sci. Lett.*, **167**, 151–165.
- Mainprice, D. & Silver, P.G., 1993. Interpretation of SKS-waves using samples from the subcontinental lithosphere, *Phys. Ear. Planet. Int.*, **78**(3–4), 257–280.
- Marson-Pidgeon, K., Savage, M.K., Gledhill, K. & Stuart, G., 1999. Seismic anisotropy beneath the lower half of the North Island, New Zealand, *J. Geophys. Res.*, **104**, 20,277–20,286.

- Martinez, F., Fryer, P. & Becker, N., 2000. Geophysical characteristics of the southern Mariana Trough, 11deg50'N-13deg40'N, *J. Geophys. Res.*, **105**(B7), 16,591–16,607.
- McKenzie, D., 1979. Finite deformation during fluid flow, *Geophys. Jour. Roy. Astr. Soc.*, **58**, 689–715.
- Nakajima, J. & Hasegawa, A., 2004. Shear-wave polarization anisotropy and subduction-induced flow in the mantle wedge of northeastern Japan, *Ear. Planet. Sci. Lett.*, **225**, 365–377.
- Nakanishi, M., Tamaki, K. & Kobayashi, K., 1992. Magnetic anomaly lineations from Late Jurassic to Early Cretaceous in the west-central Pacific Ocean, *Geophys. J. Int.*, **109**, 701–719.
- Nicolas, A. & Christensen, N.I., 1987. Formation of anisotropy in upper mantle peridotites: a review, in *Composition, Structure and Dynamics of the Lithosphere/Asthenosphere System*, pp. 111–123, ed. Fuchs, K.A.F.C., American Geophysical Union, Washington, D.C.
- Pearce, J.A., Stern, R.J., Bloomer, S.H. & Fryer, P., 2005. Geochemical mapping of the Mariana arc-basin system: Implications for the nature and distribution of subduction components, *Geochem. Geophys. Geosys.*, **6**, Q07006(7), doi:10.1029/2004GC000895.
- Pozgay, S.H., Wiens, D.A., Shiobara, H. & Sugioka, H., 2006. Seismic Attenuation Structure of the Mariana Subduction System, *EOS Trans. AGU, Fall Meet. Suppl.*, **87**(52), T23C-0504.
- Pozgay, S.H., White, R.A., Wiens, D.A., Shore, P.J., Sauter, A.W. & Kaipat, J.L., 2005. seismicity and tilt associated with the 2003 Anatahan Eruption Sequence, *J. Volcan. Geotherm. Res.*, **146**(1–3), 60–76.
- Restivo, A. & Helffrich, G.R., 1999. Teleseismic shear wave splitting measurements in noisy environments, *Geophys. J. Int.*, **137**, 821–830.
- Ribe, N.M., 1989. Seismic anisotropy and mantle flow, *J. Geophys. Res.*, **94**(B4), 4,213–4,223.
- Russo, R.M. & Silver, P.G., 1994. Trench-parallel flow beneath the Nazca plate from seismic anisotropy, *Science*, **263**(5150), 1,105–1,111.
- Savage, M.K., 1999. Seismic anisotropy and mantle deformation: what have we learned from shear wave splitting?, *Rev. Geophys.*, **37**(1), 65–106.
- Shiobara, H., Sugioka, H., Mochizuki, K., Oki, S., Kanazawa, T., Fukao, Y. & Suyehiro, K., 2005. Long term seismic observation in mariana by obss: double seismic zone and upper mantle structure, *EOS Trans. AGU, Fall Meet. Suppl.*, **86**(52), Abstract T53A-1407.
- Silver, P.G. & Chan, W.W., 1988. Implications for continental structure and evolution from seismic anisotropy, *Nature*, **335**, 34–39.
- Silver, P.G. & Chan, W.W., 1991. Shear wave splitting and subcontinental mantle deformation, *J. Geophys. Res.*, **96**(B10), 16 429–16 454.
- Smith, G.P., Wiens, D.A., Fischer, K.M., Dorman, L.M., Webb, S.C. & Hildebrand, J.A., 2001. A complex pattern of mantle flow in the Lau Backarc, *Science*, **292**, 713–716.
- Spiegelman, M. & Elliott, T., 1993. Consequences of melt transport for uranium series disequilibrium in young lavas, *Ear. Planet. Sci. Lett.*, **118**, 1–20.
- Stern, R.J., Fouch, M.J. & Klemperer, S.L., 2003. An overview of the Izu-Bonin-Mariana subduction factory, in *Inside the Subduction Factory*, p.324, ed. Eiler, J., American Geophysical Union, Washington, D.C.
- Styles, K.E., Stuart, G.W., Kendall, J.-M. & Reyners, M., 2006. Seismic anisotropy from local earthquakes in the hikurangi subduction zone, North Island, New Zealand, *EOS Trans. AGU, Fall Meet. Suppl.*, **87**(52), T23C-0510.
- Takahashi, N., Kodiara, S., Klemperer, S.L., Tatsumi, Y., Kaneda, Y. & Suyehiro, K., 2007. Crustal structure and evolution of the Mariana intra-oceanic island arc, *Geology*, **35**, 203–206.
- Teanby, N.A., 2005. E-mail, *personal communication*.
- Teanby, N.A., Kendall, J.-M. & Van Der Baan, M., 2004. Automation of shear-wave splitting measurements using cluster analysis, *Bull. Seis. Soc. Am.*, **94**(2), 453–463.
- Turner, S. & Hawkesworth, C., 1998. Using geochemistry to map mantle flow beneath the Lau Basin, *Geology*, **26**(11), 1019–1022.
- Turner, S. & Foden, J., 2001. U, Th, and Ra disequilibria, Sr, Nd and Pb isotope and trace element variations in Sunda arc lavas: predominance of a subducted sediment component, *Contrib. Miner. Petrol.*, **142**(1), 43–57.
- Van Der Hilst, R.D., Engdahl, E.R., Spakman, W. & Nolet, G., 1991. Tomographic imaging of subducted lithosphere below northwest Pacific island arcs, *Nature*, **353**, 37–43.
- van Keken, P.E., 2003. The structure and dynamics of the mantle wedge, *Ear. Planet. Sci. Lett.*, **215**, 323–338.
- Volti, T., Gorbato, A., Shiobara, H., Sugioka, H., Mochizuki, K. & Kaneda, Y., 2006. Shear-wave splitting in the Mariana trough—a relation between back-arc spreading and mantle flow?, *Ear. Planet. Sci. Lett.*, **244**, 566–575.
- Webb, S.C., Deaton, T.K. & Lemire, J.C., 2001. A Broadband ocean-bottom seismometer system based on a 1-Hz natural period geophone, *Bull. Seismol. Soc. Am.*, **91**(2), 304–312.
- Wiens, D.A. *et al.*, 2005. An Overview of the 2003–2004 Mariana subduction factory passive imaging experiment, *EOS Trans. AGU, Fall Meet. Suppl.*, **86**(52), Abstract T44A-04.
- Wüstefeld, A. & Bokelmann, G., in review. Null detection in shear-wave splitting measurements, *Bull. Seismol. Soc. Am.*, in review.
- Xie, J., 1992. Shear-wave splitting near Guam, *Phys. Ear. Planet. Int.*, **72**, 211–219.
- Yang, X., Fischer, K.M. & Abers, G.A., 1995. Seismic anisotropy beneath the Shumagin Islands segment of the Aleutian-Alaska subduction zone, *J. Geophys. Res.*, **100**(B9), 18 165–18 177.
- Zhang, S. & Karato, S., 1995. Lattice preferred orientation of olivine aggregates deformed in simple shear, *Nature*, **375**, 774–777.
- Zhang, S., Karato, S., Fitz Gerald, J., Faul, U.H. & Zhou, Y., 2000. Simple shear deformation of olivine aggregates, *Tectonophysics*, **316**, 133–152.